nature portfolio

https://doi.org/10.1038/s41586-022-05387-5

Supplementary information

Photonic flatband resonances for free-electron radiation

In the format provided by the authors and unedited

Supplementary Information
Photonic flatband resonances for free-electron radiation

Yi Yang,[1,2,*] Charles Roques-Carmes,[1,*] Steven E. Kooi,[3] Haoning Tang,[4] Justin Beroz,[1] Eric Mazur,[4] Ido Kaminer,[5] John D. Joannopoulos,[1,3] and Marin Soljačić[1,3]
[1]*Research Laboratory of Electronics and Department of Physics, Massachusetts Institute of Technology, Cambridge, Massachusetts 02139, USA*
[2]*Department of Physics, University of Hong Kong, Hong Kong, China*
[3]*Institute for Soldier Nanotechnologies, Massachusetts Institute of Technology, Cambridge, Massachusetts 02139, USA*
[4]*Harvard John A. Paulson School of Engineering and Applied Sciences, Harvard University, Cambridge Massachusetts 02138, USA*
[5]*Department of Electrical and Computer Engineering, Technion–Israel Institute of Technology, 32000 Haifa, Israel*

CONTENTS

S1. RADIATION EXPERIMENTAL SETUP

The radiation experimental setup, shown in Figure S1, is based on an upgraded modified Scanning Electron Microscope (SEM) setup (an early version of which being reported in [S1–S4]). We provide additional information on the various components of the setup, that are not shown in the main text. The polarization-insensitive beamsplitter (Element 8) sends part of the signal to a visible CCD Camera (Hamamatsu). The combination of Elements 4 (objective: Nikon CF Plan 50x/0.55 Epi ELWD), 7 (tube lens), and 9 (camera) creates an image of the sample's surface, so the location of the electron beam interaction with the sample can be visualized. The CCD provides the images shown in Section S4 and is used for optical alignment purposes. Elements 17-19 are used to scatter light off from the surface of the sample, also for alignment purposes. A set of two lenses is used (Element 12) to focus the optical signal into the fiber input feeding the spectrometer (Elements 13-16). The spectrometer is comprised of a fiber coupling into a slit, a grating turret (Element 13), and a mirror focusing the signal on an infrared InGaAs linear array (Element 16).

A. SEM Control

The SEM beam current, voltage, working distance, spot size, and stage positioning are controlled in part with the Caesium Software provided by Applied Beams LLC (Oregon). Adjustment knobs outside the SEM chamber allow to align the emitter, apertures, focusing lenses, stage rotation and tilts.

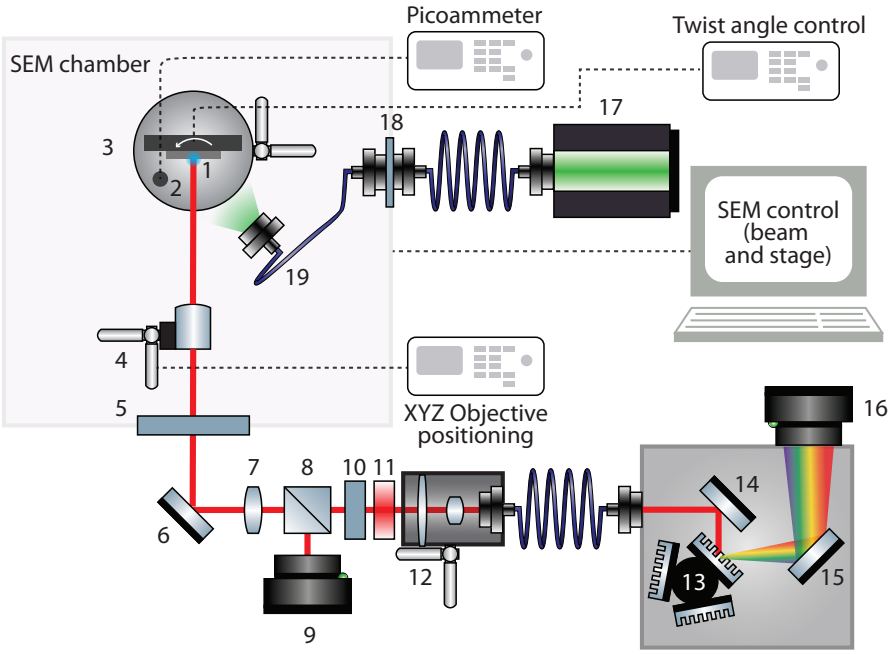

Figure S1. **Radiation experimental setup.** Inside SEM chamber: 1: Electron beam interacting with sample; 2: Faraday cup, connected to external picoammeter, measuring incident current. 3: 6-axis, fully eucentric stage, controlled by SEM control. Twist angle rotation stage. 4: XYZ objective stage. 5: X-ray blocking window. Outside SEM chamber: 6: Mirror. 7: Tube lens. 8: Beam splitter. 9: CCD Camera, imaging sample surface. 10: polarizer (optional). 11: filter. 12: XYZ cage assembly with two focusing lenses and a fiber-coupling. Inside spectrometer: 13: Grating turret. 14, 15: (Focusing) Mirrors. 16: Spectrometer InGaAs linear array. Green laser feedthrough alignment arm: 17: Green laser source. 18: Fiber-coupling feedthrough, vacuum compatible. 19: Fiber output illuminating sample.

B. Objective positioning

The XYZ positioning and tilt angle alignment of the objective (Element 4) is realized with a homemade motorized stage. The three motors are controlled through a computer interface outside the SEM chamber. Each motor is connected to an outside controller through a vacuum-preserving electronic connector.

C. Twist angle control

A rotational degree of freedom, angle θ, to the sample holder was implemented to manipulate the in-plane twist angle between the electron beam and the PhC slab. The twist angle is adjusted with a piezo motor tilt stage (range $\pm 5°$) controlled outside the SEM chamber via an electronic feedthrough. The twist angle can be read with accuracy $\pm 0.5°$ by looking through a SEM window flange.

D. Measurement protocol

A low-pass frequency filter with $\omega \lesssim 0.31$ (cut-off wavelength 1400 nm) was used to reduce incoherent cathodoluminescence near silicon's electronic band gap. Each data point (shown e.g. in Fig. 3e-g and Fig. 4a-b) was acquired over 10 s (10 averaged acquisitions which are each 1s long). Error bars, when applicable, are calculated as the standard deviation over the 10 acquisitions. For each measurement, the electron beam was positioned around the center of the camera field of view, after the XYZ position of the collection objective was optimized for maximum collection (using the motorized objective stage). The electron beam is slightly shifted off-center in the vertical direction in order to obtain maximum contrast of the peak with respect to the background at every measured energy. Background was measured as the signal from an unpatterned (unetched) sample from the same wafer. The location of the sample under electron beam exposure was regularly moved in order to reduce long-term beam exposure optical

degradation of the sample.

S2. BAND STRUCTURE MEASUREMENTS

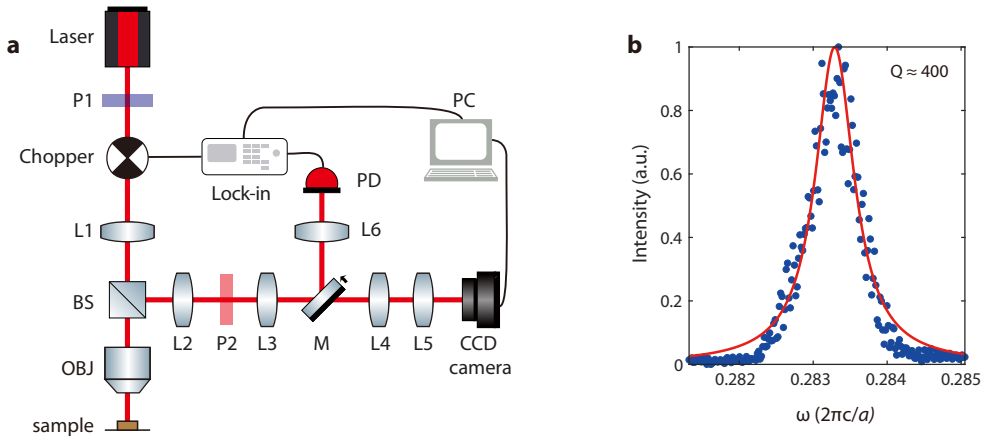

Figure S2. **Band structure measurements. a.** Optics setup. P, polarizer; L, lens; BS, beam splitter; OBJ, objective; M, flip mirror; PD, photodetector. **b.** Measured spectrum (blue dots) and its Lorentzian fitting (red line) at the flatband from optical characterization.

We used Fourier spectroscopy (Fig. S2a) to determine the band structure of the photonic crystal (PhC) slab. The photonic crystal slab was illuminated with a polarized, collimated, tunable (1500 – 1630 nm) laser beam focused by a near-infrared objective (20X Mitutoyo Plan Apo NIR Infinity Corrected Objective, NA= 0.4). For a given wavelength, we adjusted the incidence angle to match the momentum of a particular resonant pump mode. Light from that specific resonant mode was then scattered into other modes at the same frequency, as enabled by fabrication disorder. Their far-field radiation was thus resolved in momentum space as isofrequency contours. We removed the incident laser beam using a pair of crossed polarizers (P1 and P2) and then imaged the contours through a $4f$ system onto a CCD camera.

To measure the quality factor of the device, we placed a pinhole in the Fourier plane after the first $4f$ system (L2 and L3). The diameter of the pinhole is 150 µm, yielding a momentum resolution of $\delta k \approx 0.0015 \cdot 2\pi/a$. The pinhole selected specific k-points on the isofrequency contours and passed light to a photodiode. The photodiode was connected to a lock-in amplifier which was synchronized with a 1 kHz chopper placed in front of the incident laser beam. We could vary the pinhole position and record the scattered light from the lock-in amplifier to obtain the quality factor at various frequencies. The measured total quality factor of the PhC was $Q_o \approx 400$ in the vicinity of the flatband in this optical characterization (Fig. S2b).

S3. BEAM DIAMETER AND DIVERGENCE

We estimate the electron beam diameter D and divergence angle α analytically and measure the beam diameter experimentally, finding consistent results.

A. Analytical estimate

The electron beam diameter D can be estimated with the formula [S5–S7]

$$D^2 = D_0^2 + D_d^2 + D_s^2 + D_c^2 = [C_0^2 + (0.6\lambda)^2]\alpha_p^{-2} + \frac{C_s^2\alpha_p^6}{4} + \left(C_c\frac{\Delta E}{E}\right)^2\alpha_p^2. \tag{S1}$$

Here D_0 is the aberration-free Gaussian probe diameter, D_d corresponds to aperture diffraction, D_s corresponds to spherical aberration, and D_c corresponds to chromatic aberration. Our SEM uses a LaB_6

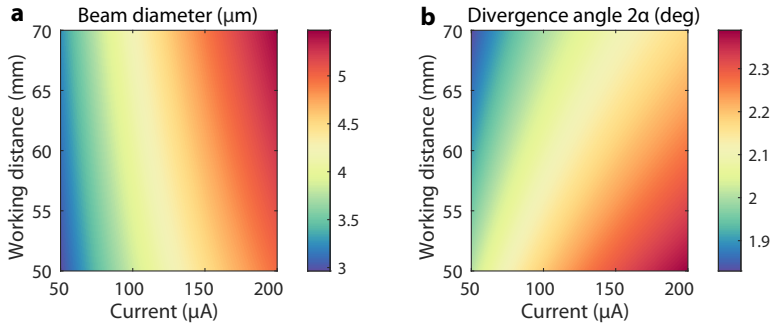

Figure S3. **Calculated beam diameter (a) and divergence angle (b) under experimental conditions.**

cathode, for the voltage regime (20–40 keV) we used, D_d and D_c are negligible [S5]

$$D^2 \approx D_0^2 + D_s^2 = C_0^2 \alpha_p^{-2} + \frac{C_s^2 \alpha_p^6}{4}, \tag{S2}$$

where

$$C_0 = \sqrt{4I/b\pi^2}, \tag{S3}$$

b is the electron gun brightness, I is the probe current, α_p is the convergence semi-angle of the electron beam, and C_s is the spherical aberration coefficient. Compared to our previous setup [S1; S2] that used a Tungsten cathode, we work with a LaB_6 cathode in our current setup that provides us electron beam of higher quality. This is reflected in the increase of the brightness b from 1×10^5 A/cm^2/sr (Tungsten) to 1×10^6 A/cm^2/sr (LaB_6) at 20 keV (see Table 2.1 in Ref. [S5]). The focal length (working distance) of our LaB_6 SEM is 50 – 70 mm, which corresponds to a spherical aberration coefficient $C_s \approx 550 - 800$ mm considering the nearly linear relation between the working distance and C_s [S5; S7]. From Eq. S2, the minimum beam diameter possible and the associated optimal convergence semi-angle are

$$D_{min} = (4/3)^{3/8} (C_0^3 C_s)^{1/4} \tag{S4}$$

and

$$\alpha_p^{opt} = (4/3)^{1/8} (C_0/C_s)^{1/4}, \tag{S5}$$

respectively. Fig. S3 shows the estimated beam diameter $D \approx 3 - 5.5$ μm and divergence angle $2\alpha_{opt} \approx 2°$ based on Eqs.(S2) and (S5) under our experimental conditions. This divergence angle puts a limit to the attainable resolution of the in-plane, twist angle between electrons and the sample.

B. Beam diameter measurements

We measured the electron beam waist experimentally, to confirm the analytical estimates provided in the previous section. The experimental setup is shown in Fig. S4: the electron beam was scanned across a sharp edge (razor blade). The scattered electrons were detected with a SEI (secondary electrons imaging) detector. An S-shaped signal was obtained as the electron beam went across the sharp edge. This signal was then fitted to an error function (integral of a Gaussian function) to extract the beam FWHM (full width at half maximum) and the corresponding beam profile. The measured beam FWHMs were in the range 4.75 – 7.63 μm and varied with the electron beam energy. The measured values are consistent with the analytical models.

Consequently, the influence of the Coulomb repulsion is negligible in our experiment. Despite the large currents and low electron energies, the relatively large beam diameter results in small Coulomb repulsion. We get an electron density of $\approx 10^{12}$ m^{-3}, corresponding to a linear density of $\approx 10^4$ m^{-1}. More generally, the beam broadening due to Coulomb repulsion can be evaluated analytically [S8]. For parameters similar to those of our experiments, the broadening is on the order of ≈ 0.1 μm which is only a fraction of the measured beam diameter.

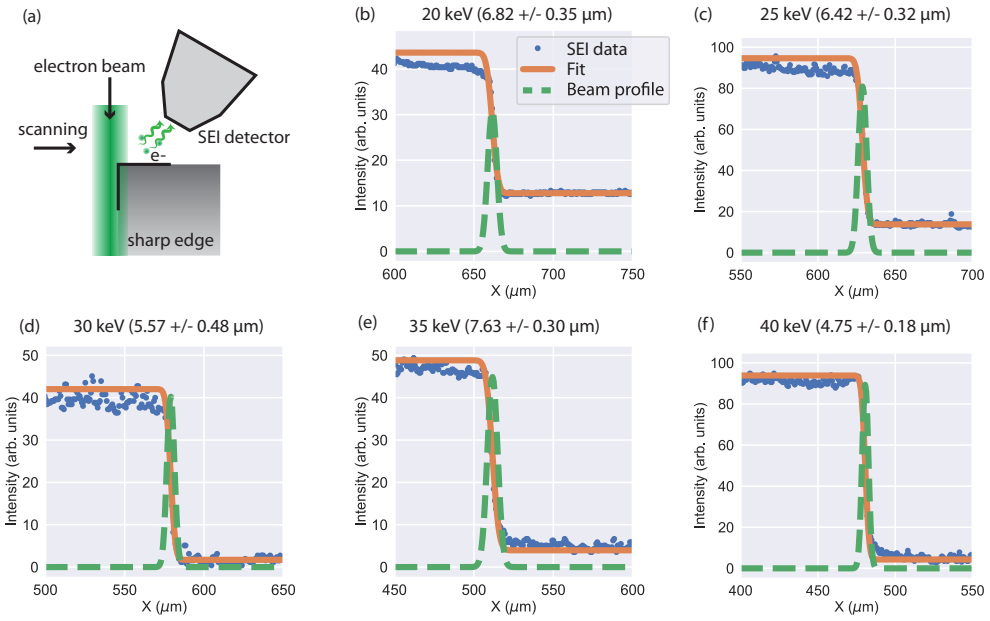

Figure S4. **Electron beam waist measurement. a.** Beam measurement setup. SEI: secondary electrons imaging. **b-f.** Beam measurement at indicated beam energy (keV). The measured beam FWHM (full width at half maximum) with uncertainty is indicated between parenthesis.

S4. COLLECTION OPTICS

A. Collection efficiency

The collection efficiency $\eta(\beta, \omega)$ can be obtained from geometrical optics. In our setup, The electron beam propagated at a small grazing angle and thus created a region that emitted most radiation in the PhC slab. We were able to control the relative translation between the objective and the light emitting region to preferentially collect radiations toward certain directions. Recall the Smith–Purcell relation for the first-order radiation

$$\sin\psi = 1/\beta - 1/\omega, \tag{S6}$$

where ψ is the polar angle from the surface normal on the longitudinal surface (i.e. surface formed by the electron velocity and the surface normal of the PhC slab) and we approximate radiation in the transverse direction, at each ψ, to be isotropic. Let ω_0 be the frequency with maximal radiation enhancement and k_0 the associated in-plane longitudinal momentum, their polar angle $\psi_0 = \sin^{-1} k_0/\omega_0$ [also see Eq. (2)] thus becomes the chief ray angle of the objective (i.e. radiation at ω_0 passes the center of the objective), which corresponds to a horizontal translation $x_0 \propto \sqrt{1-\mathrm{NA}^2}\tan\psi_0$. The collection efficiency at certain ω thus corresponds to the angle enclosed by its associated chord (red bold line in Fig. S5) on the objective (blue in Fig. S5) in its transverse radiation plane (pink surface) :

$$\eta(\beta,\omega) = \frac{2}{\pi}\tan^{-1}\frac{\sqrt{\mathrm{NA}^2 - \left(1-\mathrm{NA}^2\right)(\tan\psi - \tan\psi_0)^2}}{\sqrt{1-\mathrm{NA}^2}/\cos\psi}. \tag{S7}$$

B. Longitudinal momentum extraction

The same model for the collection efficiency also allows us to extract the k_x^{exp} for the band structure measurement from the radiation spectra by translating the electron beam in the field of view. Since the

collected radiation is limited by the numerical aperture, we can obtain the tunable chief polar angle ψ_c as

$$\psi_c = \tan^{-1}\left(\tan\psi_0 + 2\delta_x \frac{\mathrm{NA}}{\sqrt{1-\mathrm{NA}^2}}\right), \tag{S8}$$

where δ_x is the relative translation of the center of the beam (Fig. S6a and b) along the x direction, compared to the field of view. The longitudinal momentum in the experiment can thus be obtained as $k_x^{\mathrm{exp}} = \omega \sin\psi_c$ for the spectra measured at each beam position (Fig. S6).

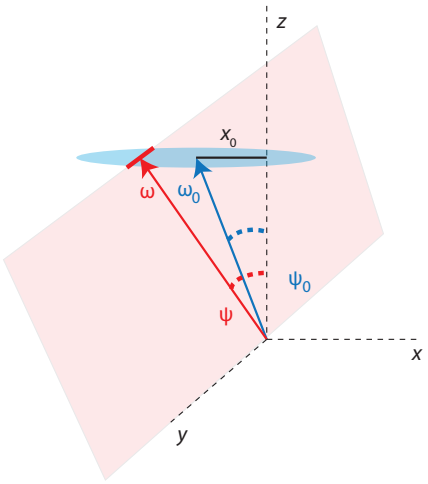

Figure S5. **Collection efficiency model.** Blue and red arrows indicates Smith–Purcell radiation at frequency ω_0 and ω into angles ψ_0 and ψ. δx is the translation in x needed to collect maximal radiation at ω_0. The collection efficiency for all ω can thus be determined via Eq. (S7).

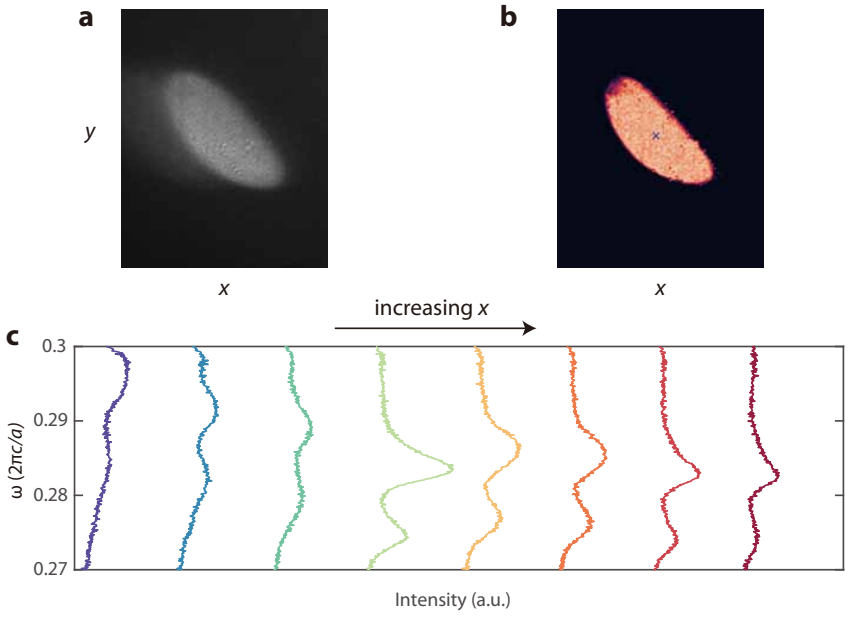

Figure S6. **Extraction of band structure by translating the position between the electron beam and the collection objective. a-b.** Raw (a) and processed (b) images from the CCD camera. The peak locations are calculated by imposing a binarization threshold filter to the raw CCD image, and measuring the mean value pixel value of the area with non-zero pixel value. **c.** Measured spectra by translating the beam along the x direction in the field of view.

S5. EXPERIMENTAL ANALYSIS

A. Shift and broadening of resonances

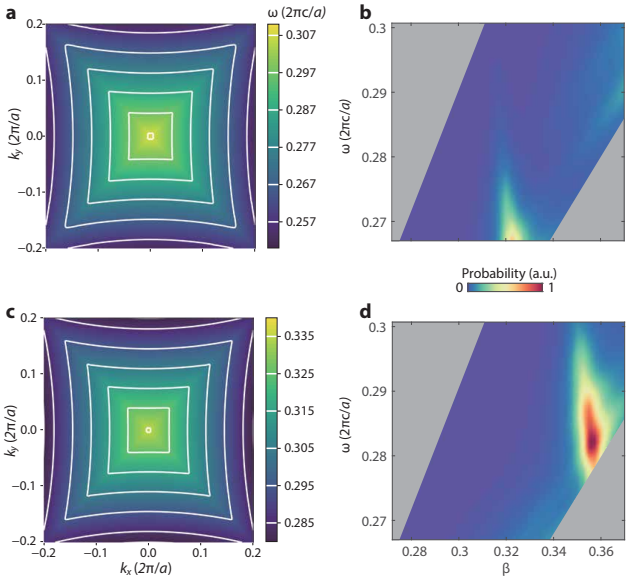

Figure S7. **Comparisons of the isofrequency contours of the PhC slab and the associated simulated radiation spectra at zero twisted angle under** $\mathrm{Re}\, n_{\mathrm{Si}} = 3.5$ **(a-b) and** $\mathrm{Re}\, n_{\mathrm{Si}} = 3.2$ **(c-d).** Shaded area in b and d are outside the numerical aperture of the objective.

We observed resonance drift and broadening when comparing the measured radiation spectra (Fig. 3 and Fig. 4) with the optical characterizations (Fig. 2 and Fig. S2; under ambient conditions), which indicates changes of the optical responses of the sample under the active, 'electron-pumped' condition in the radiation measurements. The specific observations are

1. *Resonance shift along the velocity direction.* In our optics measurement, the flatband was characterized near $k_x \approx 0.08$ (Fig. 2d). Meanwhile, the free-electron radiation measurements indicated that the flatband was near $k_x \approx 0.17$ (Fig. 3e and Fig. 4d).
2. *Resonance broadening along the frequency direction.* The quality factor of the flatband was $Q_{\mathrm{o}} \approx 400$ as in the optics measurement (Fig. S2b) while it reduced to $Q_{\mathrm{e}} \approx 50$ in the electron radiation measurement (Fig. 4a; TM-like peak).
3. *Resonance broadening along the velocity direction.* In the measurement (Fig. 3e), the enhancement region is wider along the velocity direction compared with the Smith–Purcell-only calculation (Fig. 3b).

There are a few experimental uncertainties that could contribute to the observed shift and broadening:

1. *Increase of free carriers in silicon under electron bombardment.* In our experiment, the electron beam passed above and hit onto the PhC at a grazing angle ($\psi_{\mathrm{e}} \approx 1°$). This results in an area $A \sim \pi D^2/4 \sin\psi_{\mathrm{e}} \sim 10^{-5}\,\mathrm{cm}^2$ under electron bombardment. Recall that the current operates on the order of $\sim 100\,\mu\mathrm{A}$, a high concentration of free carriers was injected into the light-emitting region of the silicon PhC slab and thus modified its optical responses.
2. *Temperature rise in materials.* Electron bombardment could also cause local temperature rise on the sample. *

---

* Since we did not observe melting of silicon (melting point $\approx 1700\,\mathrm{K}$), the local temperature rise should be on the order of $10^2 - 10^3\,\mathrm{K}$, which translate into a linear refractive index shift $0.01 - 0.1$ at maximum considering silicon's thermal conductivity.

3. *In-plane momentum spread due to beam divergence* In contrast to point electrons in the modelling, the electron beam in the experiment was not perfectly collimated and had a divergence angle $\approx 2^\circ$ (Sec. S3). The Coulomb repulsion from the charged area on the sample could cause additional divergence to the electron beam in the vicinity of the sample. [†]
4. *Surface oxidization.* Silicon forms an intrinsic oxide layer of a few nanometer thick under ambient conditions [S9]. The oxide layer may become thicker when the ultraviolet-ozone cleaning treatment was applied to the sample. [‡]
5. *Surface contamination.* Remaining hydrocarbon molecules in the vacuum chamber could deposit onto and thus contaminate the sample surface during the radiation measurement. [§]

B. Effective doping of silicon

Out of the uncertainties enumerated above, the chief reason to the observed resonance shift and broadening along the frequency direction is the modifications to the optical properties of silicon under direct electron beam exposure and bombardment. Electrons could enter the PhC slab and caused an effective increase of the doping level in silicon, which rendered the material more conductive and optically absorptive.

The optical properties of silicon under different doping levels have been investigated previously (e.g. see Refs. [S11; S12] and references therein). Intuitively, the scenario could be understood by the Drude model. An increase of the doping level causes a decrease in $\mathrm{Re}\, n_{\mathrm{Si}}$ and an increase in $\mathrm{Im}\, n_{\mathrm{Si}}$ simultaneously (where n_{Si} is the refractive index of silicon), as consistent with the Drude picture. Compared to its intrinsic refractive index ~ 3.5 in the near-infrared regime, n_{Si} could reduce to $\sim 2 + 1\mathrm{i}$ near 2 μm, which is highly absorptive, under a high doping concentration $\sim 10^{21}\ \mathrm{cm}^{-3}$ [S11].

In our measurement inside a modified scanning electron microscope, the instantaneous refractive index of our sample under simultaneous beam exposure could not be measured in-situ, which makes it challenging for theoretically calculating the associated radiation spectra shown in Fig. 3b and d. In these calculations shown in the main text, alternatively, we choose $n_{\mathrm{Si}} = 3.2 + 0.03\mathrm{i}$, which corresponds to an effective doping concentration $10^{20} - 10^{21}\ \mathrm{cm}^{-3}$ based on previous studies [S11; S12]. The material dispersion of the index of silicon is neglected because the relevant frequency window in our measurement is narrow.

We compare the calculated isofrequency contours under $\mathrm{Re}\, n_{\mathrm{Si}} = 3.5$ and $\mathrm{Re}\, n_{\mathrm{Si}} = 3.2$ in Fig. S7a and c. Under a smaller refractive index, the band moves toward higher frequencies. Such modifications to the band structure are reflected in the calculated radiation spectra. As shown in Fig. S7b and d, the 'resonant' velocity, shown by the peak enhancement of radiation, moves from $\beta \approx 0.32$ ($\mathrm{Re}\, n_{\mathrm{Si}} = 3.5$) to $\beta \approx 0.35$ ($\mathrm{Re}\, n_{\mathrm{Si}} = 3.2$).

C. Broadening along the velocity direction

Two major reasons could explain the observed enhancement broadening along the velocity axis in Fig. 3.

1. *Temporal and spatial fluctuation of carriers.* In our theoretical calculations, we assume a simple constant modification to n_{Si} as described above. However, in the experiment, n_{Si} had extra temporal and spatial dependence which could stem from a variety of factors including the density distribution of the electron beam, the Coulomb repulsion between the electron beam and the charged sample surface, and the diffusion of electrons inside the sample. Therefore, the theoretical treatment—constant modification to n_{Si}—should be understood as the zeroth-order expansion of $n_{\mathrm{Si}}(\mathbf{r}, t)$. The

---

[†] The beam divergence, although relevant to the enhancement broadening, should contribute negligibly to the resonance shift.

[‡] As the surface oxidization is self-limiting, the oxide thickness of silicon is still less than tens of nanometers even under hours of high-temperature oxidization process [S10], compared to which the oxidization in our case should be much milder.

[§] The accumulation of surface contamination occurred at a much longer time scale than the other factors listed above and our data collection.

fluctuation of n_{Si}, in both space and time, could contribute to the broadening of the enhancement region along the velocity β direction in our measurements.

2. *Concurrent radiation pathways.* As the electron beam was launched at a nonzero grazing angle, electrons also impinged onto the sample. Therefore, aside from Smith–Purcell radiation, other radiation pathways [S13], predominantly incoherent cathodoluminescence (ICL), could occur simultaneously. These types of radiation could also get enhanced by the flatband with less sensitivity on electron velocity because of their localized nature (in contrast to the extended nature of Smith–Purcell radiation).

Below, we include a quantitative analysis to elucidate contributions from different radiation processes in our measured $\theta \approx 0°$ data (Fig. 3e). When free electrons enter silicon, the resulting ICL is dominantly stronger than transition radiation for the electron energies and spectral range in our experiments [S13]. Therefore, we ignore transition radiation and focus on the localized ICL and the extended Smith–Purcell radiation in the following analysis. We model the total measured radiation $S(\beta, \omega)$ as

$$S(\beta, \omega) = c_1 S_{\mathrm{SP}}(\beta, \omega) + c_2 S_{\mathrm{ICL}}(\omega), \tag{S9}$$

where the first and second term correspond to Smith–Purcell (SP) radiation (Fig. 3b) and ICL (Fig. 3c), respectively and $c_{1,2}$ are coefficients to be determined. ICL is a complex, multi-physics process involving energy levels of materials and defects (requiring density functional theory calculations) and fluctuational electrodynamics. Here, for simplicity, we adopt a single Lorentzian fitting for ICL; meanwhile, we assume a negligible velocity dependence in $S_{\mathrm{ICL}}(\omega)$ because of ICL's localized nature:

$$S_{\mathrm{ICL}}(\omega) \propto \frac{\Gamma^2}{(\omega - \omega_0)^2 + \Gamma^2}, \tag{S10}$$

where ω_0 is the center frequency and 2Γ is the full width at half maximum.

We perform a least-squared fitting on four parameters $\{c_1, c_2, \omega, \Gamma\}$ via

$$S_{\mathrm{exp}}(\beta, \omega) \sim S(\beta, \omega | c_1, c_2, \omega_0, \Gamma), \tag{S11}$$

where $S_{\mathrm{exp}}(\beta, \omega)$ is the experimental data at zero twisted angle (Fig. 3e). The fitted parameters are $\widehat{c_1} = 0.713 \pm 0.010$, $\widehat{c_2} = 0.343 \pm 0.004$, $\widehat{\omega_0} = 0.285 \pm 0.00005$, and $\widehat{\Gamma} = 0.004 \pm 0.00007$, where $\widehat{c_1}$ and $\widehat{c_2}$ are in dimensionless units, $\widehat{\omega_0}$ and $\widehat{\Gamma}$ are in unit of $2\pi c/a$, and the uncertainty corresponds to 95% confidence internal. The fitted result is shown in Fig. 3d, which achieves an improved agreement with the measured data in Fig. 3e.

Furthermore, our twist-angle measurements also offer additional corroborations for the analysis above. Since the flatband-enhanced Smith–Purcell radiation depends crucially on momentum, the remaining enhancements at ±5° (Fig. 3e and f) are ICL-dominant. Therefore, the following relation holds

$$\frac{\text{Enhancement at } \pm 5° \text{ twist angle}}{\text{Enhancement at zero twist angle}} \sim \frac{\widehat{c_2}}{\widehat{c_1} + \widehat{c_2}} \approx 0.325 \pm 0.006. \tag{S12}$$

This estimated ratio is also accordant with our experimental observations, where the 10^2-fold enhancement at zero twist angle reduce to about 30-fold at ±5° (see Fig. 3f-g).

D. Enhancement evaluation

We use the ratio between the peak radiation and the average radiation in the off-flatband region to quantify the intensity enhancement Λ:

$$\Lambda \sim \frac{\max \mathrm{S}(\beta, \omega)}{\iint_A S(\beta, \omega)\ \mathrm{d}\beta\ \mathrm{d}\omega \,/\, \iint_A \mathrm{d}\beta\ \mathrm{d}\omega}, \tag{S13}$$

where $A = (\beta < 0.32, \omega < 0.28)$ is a parameter space about 10% off the flatband, which is comparable to the case shown in Fig. 2e and f. Compared with the idealized lossless case where $\Lambda \sim 1 \times 10^6$ (i.e. the comparison between Fig. 2e-f and Fig. 2i-j), the incorporation of the electron-induced material loss reduces Λ to ≈ 200 and ≈ 100 for the numerical and experimental results, respectively (Fig. 3b-e).

S6. PHYSICAL MECHANISM OF ENHANCED INTERACTION

In this section, we provide intuitions for the enhanced electron-light interaction and connect it to Purcell factor and spectral density of states. As shown in Ref. [S14], the radiation in a photonic crystal (assuming two-dimensional without loss of generality) is given by

$$\frac{\mathrm{d}\Gamma(\omega)}{\mathrm{d}x} \propto \int_{\partial\mathbf{k}} \frac{|a(\omega,\mathbf{k})|^2}{\nabla_{k_\perp}\omega_{\mathbf{k}}}\,\mathrm{d}k_\perp \tag{S14a}$$

$$= \int_{\partial\mathbf{k}} \frac{|a(\omega,\mathbf{k})|^2}{v_g^\perp(\omega,\mathbf{k})}\,\mathrm{d}k_\perp, \tag{S14b}$$

where the lefthand side is the emission probability per unit length, $\partial\mathbf{k}$ is the intersection between the photonic band and the electron surface, $a(\omega,\mathbf{k})$ is the mode amplitude, $k_\perp$ is the transverse momentum, and $v_g^\perp(\omega,\mathbf{k})$ is the transverse component of the group velocity. Here we also assume single-band condition.

The resonant field enhancement [S15] is well established under the coupled mode theory:

$$\frac{|a(\omega,\mathbf{k})|^2}{|a_0(\omega,\mathbf{k})|^2} \propto \frac{Q_{\mathrm{tot}}(\omega,\mathbf{k})}{Q_{\mathrm{rad}}(\omega,\mathbf{k})}\frac{Q_{\mathrm{tot}}(\omega,\mathbf{k})}{V_{\mathrm{eff}}(\omega,\mathbf{k})} = \eta(\omega,\mathbf{k})F_{\mathrm{tot}}(\omega,\mathbf{k}) \equiv F_{\mathrm{rad}}(\omega,\mathbf{k}) \tag{S15}$$

Here $a_0(\omega,\mathbf{k})$ is the field amplitude in the absence of the resonance, V_{eff} is the effective volume, η is radiative efficiency, F_{tot} is the total Purcell factor, F_{rad} is the radiative Purcell factor, Q_{rad}, Q_{abs}, and Q_{tot} are the radiative, absorptive, and total quality factors, respectively. Aside from absorptive loss from materials, practically Q_{abs} also takes into account disorder scattering from fabrication imperfections even for lossless materials (like silicon as in our case). In general, the Q-matching $Q_{\mathrm{rad}} = Q_{\mathrm{abs}}$ condition enables the optimal field enhancement [S15].

Inserting Eq. (S15) into Eq. (S14), we get the radiation enhancement

$$\frac{\mathrm{d}\Gamma(\omega)/\,\mathrm{d}x}{\mathrm{d}\Gamma_0(\omega)/\,\mathrm{d}x} \underset{\sim}{\propto} \int_{\partial\mathbf{k}} \frac{F_{\mathrm{rad}}(\omega,\mathbf{k})}{v_g^\perp(\omega,\mathbf{k})}\,\mathrm{d}k_\perp. \tag{S16}$$

Here $\Gamma_0(\omega) \propto \int_{\partial\mathbf{k}}|a_0(\omega,\mathbf{k})|^2\,\mathrm{d}k_\perp$ is the initial emission rate without the flatband enhancement. Note that Eq. (S16) assumes weak dependence of $a_0(\omega,\mathbf{k})$ on $\mathbf{k}$. In order to get an intuitive picture that connects with density of states, we further assume that the contributing resonances (e.g. the resonance continuum of a flatband along the transverse direction) have similar Purcell factors $F_\perp(\omega)$, which can be taken out of the integral. Eq. (S16) can thus be further simplified into a figure-of-merit:

$$\frac{\mathrm{d}\Gamma(\omega)/\,\mathrm{d}x}{\mathrm{d}\Gamma_0(\omega)/\,\mathrm{d}x} \underset{\sim}{\propto} F_\perp(\omega)\int_{\partial\mathbf{k}} \frac{1}{v_g^\perp(\omega,\mathbf{k})}\,\mathrm{d}k_\perp \propto F_\perp(\omega)\cdot\mathcal{S}_\perp(\omega), \tag{S17}$$

where $\mathcal{S}_\perp(\omega)$ (note that the integral in Eq. (S17) is an expression that follows the definition of density of states [S16]) is the projected density of states along the transverse direction of electron velocity. Evidently, both the transversely-projected Purcell factors and the transversely-projected spectral density of states contribute to the enhanced radiation.

S7. NUMERICAL METHODS

The photonic band structure in Fig. 2b is calculated using a finite-difference time-domain MEEP package [S17]. Numerical radiation probability is obtained via the frequency-domain calculation in the RF module in COMSOL Multiphysics. External fields of point electrons are modelled with line currents at each frequency. Radiation probability, under each electron velocity and at each frequency, is obtained by taking a surface integral of the Poynting vector above the photonic crystal slab. The wavevector component analysis in Fig. 2e-j is obtained by taking the Fourier transform of the real-space radiation. Since k_x is determined by the electron velocity, k_y and k_z are constraint by the following relation $k_y^2 + k_z^2 = \sqrt{\omega^2 - k_x^2} = 2\omega/\beta - \omega^2/\beta^2\gamma^2 - 1$ where $\beta = v/c$ is the electron velocity, and $\gamma = 1/\sqrt{1-\beta^2}$ is the Lorentz factor.

S8. DISTINCTION BETWEEN SHEET ELECTRONS AND POINT ELECTRONS

In reality, almost all electron sources generate point electrons; the generation of electron sheet beams is possible in principle, but is experimentally challenging, requiring electron beam shaping that relies on substantial electron optics and precise control despite space charge at high flux configurations. Nevertheless, sheet electron beams are widely used as a mathematical convenience that reduces computational complexity in modeling free-electron radiation sources [S18–S22]. By leveraging this mathematical convenience, the transverse momentum is neglected, and the transverse momentum mismatch highlighted in our main text disappears. Because of this theoretical simplification, the predicted radiation could fall substantially short in realistic three-dimensional settings.

We elaborate on this aspect using a numerical comparison below. We consider the enhancement of free-electron radiation from a bound state in the continuum (BIC) [S23], a topological defect in momentum space. In Ref. [S1], this scheme was introduced via the coupling between a sheet electron beam and a BIC of a one-dimensional grating (Fig. S8a). As shown in Fig. S8b and stated in Ref. [S1], a sheet electron beam (which is translationally invariant along the y direction) is needed to achieve a divergent emission probability near the BIC. In contrast, the enhancement reduces to about one order of magnitude (Fig. S8d) for the same structure under point-electron excitation (Fig. S8c), as a result of the transverse momentum mismatch described in our manuscript.

Importantly, the flatband scheme presented here proposes an avenue to recover the diverging enhancement (as in Fig. S8b) with point electrons—coupling them with a judiciously-designed flatband of BIC arc (e.g. based on the method described in Ref. [S24]).

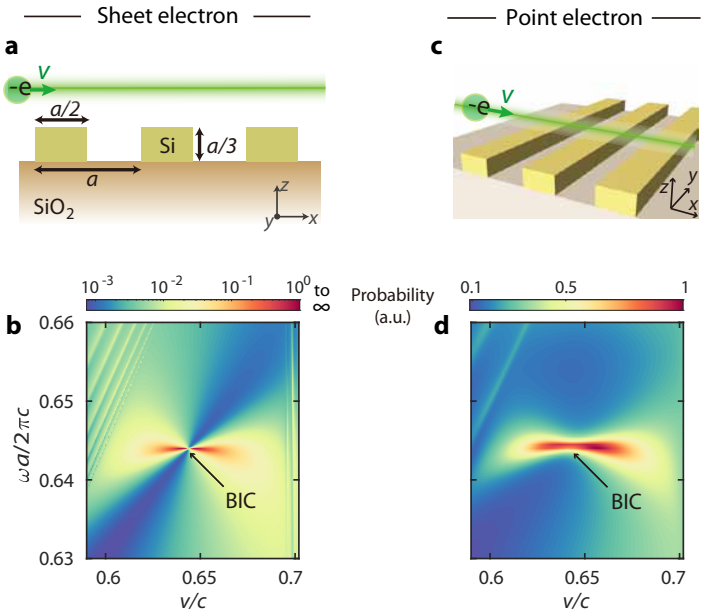

Figure S8. Enhancement comparison between sheet-electron and point-electron excitation of a point-BIC in momentum space. a-b. A schematic drawing (a) of a sheet electron beam coupling with a silicon-on-insulator grating (1D photonic crystal slab: periodic in x and infinite in y) and the associated emission probability near its BIC (b; in logarithmic scale). **c-d.** Same as a and b but for point electron excitation. d is in linear scale and open boundary condition is imposed onto the transverse y direction. Practically, fabrication disorder and material absorption reduce the extent of enhancement in both cases, but their contrasting behaviors shown here still hold.

S9. POINT AND LINE DEGENERACIES BETWEEN ELECTRON SURFACE AND PHOTONIC BAND

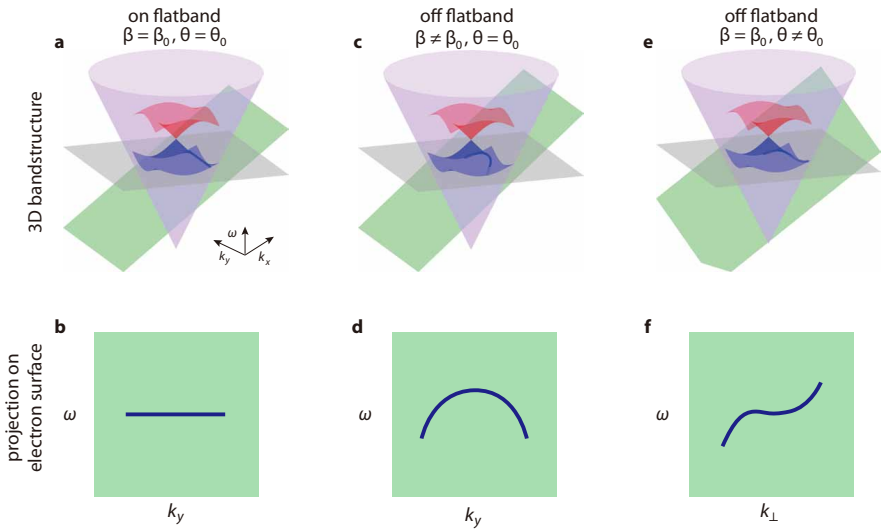

Figure S9. **Coupling the electron surface (green) with the flatband requires the control of the electrons' velocity $\beta = v/c$ and their in-plane twist angle θ with photonic crystal slab. a-b.** At a certain velocity β_0 and a certain twist angle θ_0, the intersection (solid blue line) becomes flat and thus forms a line degeneracy with the associated isofrequency surface, which substantially enhances electron-light interaction and free-electron radiation. In our case, $\theta_0 = 0$ because the flatband is perpendicular to the $\Gamma - X$ direction. **c-d.** At other velocities $\beta \neq \beta_0$, the intersection on the electron surface (green) is non-flat, rendering point degeneracies with an isofrequency surface (grey). **e-f.** At other twist angles $\theta \neq \theta_0$, free electrons and the PhC slab form a moiré systems, resulting in a relative twist between the photonic bands and the electron surface. Therefore, the intersection also becomes non-flat. The light cone is in purple and photonic bands are shown in red and blue. In f, $k_\perp = |-k_x \sin\theta\hat{x} + k_y \cos\theta\hat{y}|$.

S10. ANGLES OF ENHANCED RADIATION

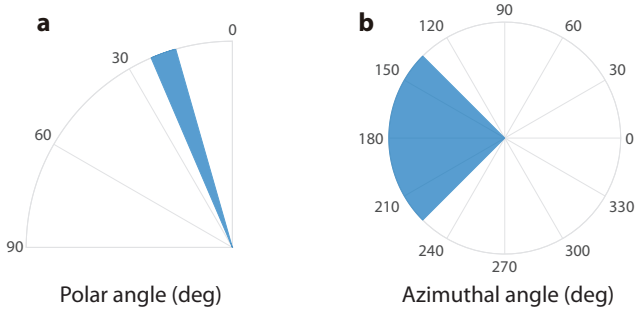

Figure S10. **Polar (a) and azimuthal (b) angles of the enhanced radiation.** Blue shading indicate the angles of enhanced radiation from the flatband resonances, which is characterized in Fig. 2 of the main text. Electron velocity is chosen as v_+.

Radiation is selectively enhanced toward directions determined by the flatband momenta. Specifically, as shown in Fig. S10, enhanced radiation becomes strongly directional towards polar angles $\sin^{-1} c\sqrt{k_0^2 + k_y^2}/\omega_0$ and azimuthal angles $\tan^{-1} k_y/k_0$, where $k_y \in [-k_0, k_0]$, k_0 is the flatband momentum in the longitudinal direction, and c is the speed of light in vacuum.

S11. FLATBAND-INDUCED LOCALIZATION

A unique aspect of flatbands is their ability to support localization. Under free-electron excitation, the localization is anisotropic and its characteristics are:

Delocalization along the longitudinal direction: Because the longitudinal momentum is always determined by $k_{||} = \omega/v$ (where ω is frequency and v is electron velocity), optical fields are always extended, i.e. no localization, along the trajectory of free electrons.

Localization along the transverse direction: Because free electrons couple to a continuum of transverse momenta, localization can appear along that direction. As the transverse flatband may not enclose the full Brillouin zone (as shown in Fig. 2b and d), the transverse localization can exhibit a decay length spanning many unit cells, which is proportional to the inverse of the length of the flatband in momentum space.

We include a numerical example to directly visualize the flatband-induced localization. Specifically, we consider the free-electron radiation in a two-dimensional (2D) photonic crystal PhC (Fig. S11). This dimension reduction from three-dimensional (3D) PhC slabs maintains the same flatband characteristic (compare Fig. S11b with Fig. 2b) while decreases the computational complexity such that a many-unit-cell simulation becomes computationally feasible. The comparison between Fig. S11c and d clearly shows the localization of light fields because of the flatband.

Therefore, our work presents a flatband-based concept for electron interaction: free electrons can excite and interact with localized modes in a transversely periodic structure. It is precisely the nature of flatbands that makes this possible.

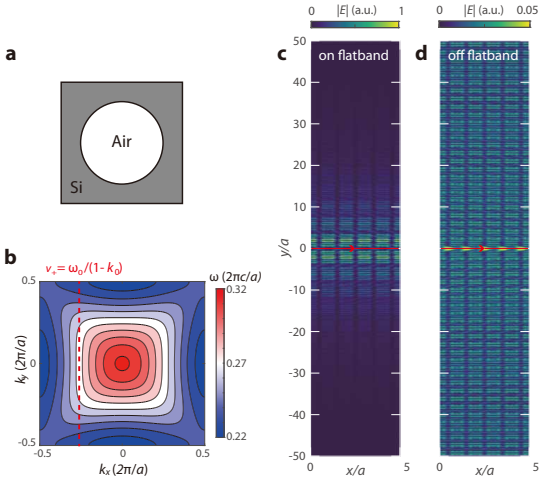

Figure S11. **Flatband-induced localization under free-electron excitation. a.** Geometry of the 2D PhC with an air-hole filling ratio of 0.36, same as the cross-section of the PhC slab in our experiment. **b.** Isofrequency contour of the second lowest TE (E_x, E_y, H_z) mode. Flatband appears near $\omega \approx 0.27$. Resonant coupling with v_+ is indicated by the red dash line. **c-d.** Localized (c; on-flatband condition) and delocalized (d; 3% off-flatband condition) field profiles at $\omega \approx 0.27$. Red lines indicate electron trajectory.

S12. NUMERICAL COMPARISONS WITH DIFFRACTIVE GRATINGS

In Fig. 2 in the main text, order-of-magnitude radiation enhancement is predicted from the comparison between on- and off-flatband conditions of the same structure. In this section, complementarily, we compare the on-flatband radiation from the PhC slab and the conventional Smith–Purcell radiation from a diffractive grating.

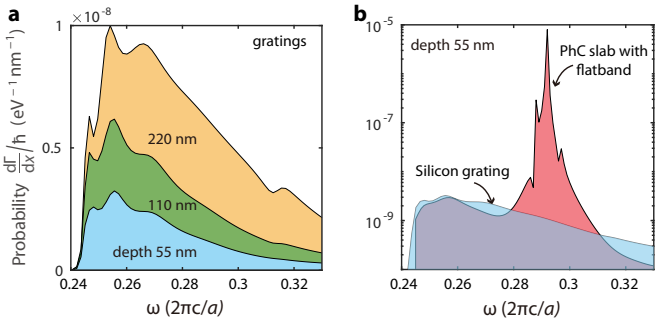

Figure S12. Comparison between Smith–Purcell radiation from grating diffraction and from a PhC flatband. **a.** Moderate increase of radiation with deeper gratings. **b.** Substantially enhanced on-flatband radiation compared with that of the grating with the same depth 55 nm. The off-flatband radiation (e.g. at a detuned frequency $\omega \approx 0.26$) from the PhC is similar to that of the grating. Here, silicon gratings are assumed with a 50% duty cycle. Periods of all structures are fixed at 430 nm (same as that of our experimental sample). Electron-structure separation is fixed at 200 nm.

Specifically, we numerically compare the Smith–Purcell radiation from gratings of various depth with that from the flatband scheme, which is shown in Fig. S12. In Fig. S12a, radiation intensity can be improved by increasing the depth of the grating, almost at a linear scale. Eventually, the radiation intensity should saturate for grating depth larger than the decay length of the electrons' external fields. In Fig S12b, order-of-magnitude enhancement can be seen by comparing the radiation from the PhC flatband (red) with that from the grating of the same depth (blue; same as the blue plot in Fig. S12a). Notably, the off-flatband radiation at detuned frequencies is comparable to that of the grating. If we compare the flatband radiation from a shallow PhC (red in Fig. S12b) with that from a deeper grating (yellow in Fig. S12a), substantial enhancement is still maintained.

At last, it is noted that we etched our PhC slab in a shallow manner for maintaining the desired band flatness and lowering the band frequency for phase matching with free electrons of finite energy (≤ 40 keV). Because we have shown in Sec. S6 that the enhancement mechanism does not depend on material or geometry details, stronger absolute emission can be achieved if we apply the flatband scheme to deeply-etched structures, which are beyond the design space of our experiment.

S13. EXPERIMENTAL COMPARISONS WITH DIFFRACTIVE GRATINGS

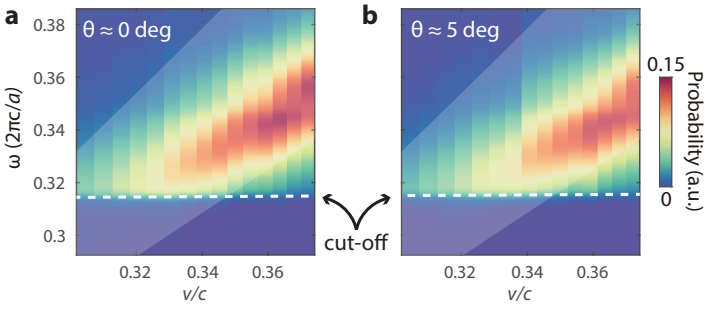

Figure S13. Lack of twist-angle dependence in measured Smith–Purcell radiation from a grating: measured similar radiation intensity under the untwisted (a) and twisted (b; twist angle 5 degree) conditions. The grating is made entirely of silicon with a period of 500 nm, depth of 350 nm, and a duty cycle of 0.44. White shading region indicates the collected Smith–Purcell regime limited by the numerical aperture of the objective. We replaced the Nikon CF Plan 50x/0.55 Epi ELWD objective with a Nikon Tu Plan Fluor 10x/0.3 objective to increase the signal-to-noise ratio because the emission from the grating was much weaker than that from the PhC. Radiation from the grating is calibrated by the magnification ratio of the two objectives and normalized by the maximal measured radiation from the PhC slab. White dashed line shows the cut-off frequency of the spectrometer.

To confirm the resonant nature of the flatband enhancement in Fig. 3, we performed experimental comparisons with silicon gratings. In the main text, we show that the radiation from the PhC's flatband is nearly 30-fold stronger than that from the a 150 nm-depth grating (Fig. 3h). Here we provide extra experimental evidence using a 350 nm-depth grating (Fig. S13), which exhibits increased radiation intensity because of its deeper grooves. Nevertheless, the radiation from the PhC's flatband (Fig. 3e) is still about 7-fold stronger, despite that the PhC slab's depth is about 7-fold shallower.

Moreover, the twist-angle dependence of radiation intensity, as seen in our PhC slab sample, does not appear between different tilted angles of the grating for the lack of flatband resonances (Fig. S13). Instead, slightly frequency-detuned emission peaks of similar intensities are expected only because electrons 'see' a longer effective period; these observations are accordant with the standard Smith–Purcell radiation.

We note that the measured enhancement (compared to gratings) fell short of the theoretical predictions (Sec. S12), again due to the increased losses in silicon under electron beam exposure at a nonzero incident angle.

S14. GENERALITY OF THE FLATBAND SCHEME

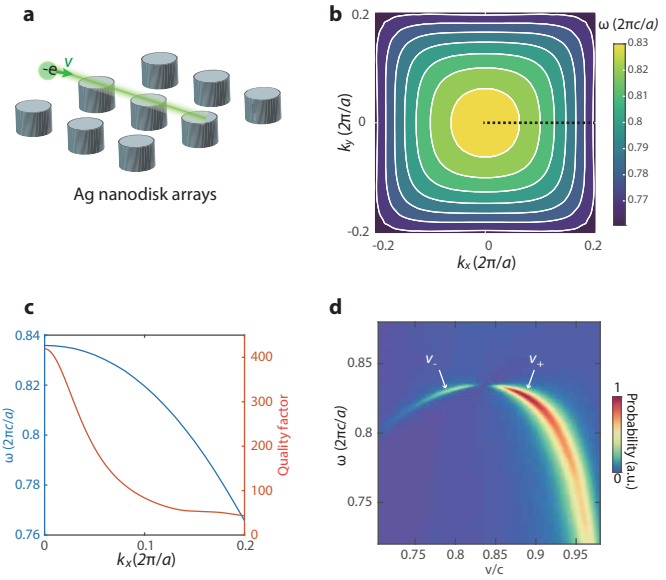

Figure S14. **Enhancement of free-electron radiation from the flatband of a plasmonic crystal. a.** Schematic.The plasmonic crystal is a Ag nanodisk array with periodicity $a = 600$ nm, depth 200 nm, and a filling factor of 0.15. The permittivity of Ag (in the visible and near-infrared regimes) is taken from the tabulated data in Ref. [S25]. **b.** Isofrequency contour of the TM-like (H_x, H_y, E_z) band of interests. Flatbands appear in a similar fashion as that in our silicon-based sample in Fig. 2 of the main text. **c.** Line cut (dotted line in b) of the contour along the $\Gamma - X$ direction: band dispersion $\mathrm{Re}\,\omega$ (blue) and the associated quality factor $Q \equiv \mathrm{Re}\,\omega/2\,\mathrm{Im}\,\omega$ (red). For this structure, Q drops quickly away from Γ point. **d.** Calculated radiation spectra under various velocities. The optimal resonant velocities $v_\pm$ also appears near the flatbands, but detune towards the Γ point because of the emission enhancement's dependence on Q [red curve in c and also see Eqs. (S16) and (S17)].

The flatband scheme is general. First, it applies to almost any material systems that permit the design of flatbands in any photonic geometries. Therefore, enhancements are expected in a wide range of platforms, ranging from insulators, semiconductors, and metals. We performed experiments on silicon photonic crystal slabs because of the availability of large-area nanopatterning techniques. Second, aside from electrons, composite charges could be combined with the scheme for superradiance. Third, the flatbands can be made of guided modes, resonances, or even bound states in the continuum. We elaborate on each point below.

Material platform: A numerical calculation of emission enhancement from a flatband in a plasmonic lattice (Fig. S14), complementary to our silicon-on-insulator lattice in the main text, is in-

cluded to demonstrate this point below. Evidently, Similar flatband-induced enhancements appear (Fig. S14d).

Superradiance: Superradiance is a many-body emission phenomenon that can be caused by either pre-bunched electrons or self-bunched electrons. Pre-bunched superradiance is a complementary method that could be used in junction with the flatband scheme proposed here, while self-bunched superradiance could be enabled by the flatband in the stimulated regime.

Our work lies within the linear-response, spontaneous regime, the radiation scales linearly with the beam current, and the flatband enhancement [Eq. (S16)] applies to any charged particles and also composite charges. Pre-bunched electrons can be prepared to exhibit spatially coherence among individual electrons such that they behave collectively as composite particles. Pre-bunched electrons can also interact with flatbands with the enhancement given by:

$$\frac{\mathrm{d}\Gamma_{\mathrm{bunch}}(\omega)/\ \mathrm{d}x}{\mathrm{d}\Gamma_{\mathrm{single}}(\omega)/\ \mathrm{d}x} = n_e\left[1 + (n_e - 1)|f|^2\right], \tag{S18}$$

where n_e is number of electrons, f is the bunching factor (see Ref. [S26]), and Γ_{bunch} and Γ_{single} are the bunched-electron and the single-electron emission probabilities, respectively. Evidently, Superradiance from perfectly prebunched electrons with $|f| = 1$ scales with n_e^2, which offers an n_e enhancement to the spontaneous emission from n_e numbers of single point electrons. Therefore, pre-bunched superradiance can be combined with the flatband scheme to provide stronger total enhancement, i.e. the product between Eqs. (S16) and (S18).

Superradiance from self-bunched electrons can be more complicated. In this process, many electrons of the beam, initially in random positions, couple to the mode collectively, which results in spatial coherence, i.e. bunching, after some interaction lengths. Many previous theoretical works have shown that sheet electron beams coupling with guided modes [S20–S22] or a zero-dimensional BIC (short for 'bound states in the continuum') [S27] could generate superradiance in Smith–Purcell radiation. It is thus reasonable to conjecture that the flatband scheme could be useful for generating self-bunched superradiance with point electrons, which would be helpful for relaxing the requirements of the current and quality of the electron beam in experiments.

BIC-electron radiation: This BIC enhancement method could be incorporated into the flatband scheme. In Ref. [S1], an isolated BIC point (i.e. a zero-dimensional BIC in momentum space) enables a strong enhancement of free-electron radiation under sheet beam excitation, which, nevertheless, could be challenging to prepare experimentally. For point electrons that are more practical, one should create a flatband of BICs (i.e. a one-dimensional BIC arc) along the transverse momentum, as we demonstrated using flatband resonances (rather than BICs) in this work. Thus, an enticing direction would be pursuing stronger enhancements by generalizing the flatband scheme with one-dimensional BIC arcs, which have been recently shown possible by environmental design [S24; S28].

S15. FLATBAND RESONANCES FOR STRONG COUPLING AND ACCELERATORS

The enhanced far-field radiation, as we observed in this work, also relates to the improved near field (due to the excitation of the flatband continuum) that can strongly act back onto free electrons. Therefore, the flatband scheme can be leveraged to achieve large values of electron-photon coupling. We will elaborate on this point using the recently-developed dimensionless quantum-mechanical coupling strength g_{Qu} and relate it to free electron accelerators.

g_{Qu} quantifies the dimensionless interaction strength between the electron and light [S29; S30]: $|g_{\mathrm{Qu}}|^2$ is the Poisson parameter of free-electron radiation which indicates the number of spontaneously emitted photons per single electrons. Evidently, $|g_{\mathrm{Qu}}| \gtrsim 1$ indicates a nonperturbative strong-coupling regime between free electrons and photons. In this regime, an emitted photon can act back on electrons, which further leads to non-negligible multi-photon emission and absorption.

Notably, regardless of the level of external optical pumping (as in dielectric laser accelerators), g_{Qu} is an intensive parameter of photon-electron interaction that can be evaluated from 'cold' cavities: $|g_{\mathrm{Qu}}|^2 = \int \Gamma(\omega)\ \mathrm{d}\omega$, where $\Gamma(\omega)$ is the coherent cathodoluminescence (such as Smith–Purcell radiation considered here; distinct from the incoherent cathodoluminescence discussed in Sec. S5.C) probability.

Let us consider the numerical example on the flatband scheme in Fig. S15. For an electron-structure separation of 100 nm, which is achievable with state-of-the-art ultrafast electron micoscopes, the integration of the emission spectrum (Fig. S15a) yields a probability of $2 \times 10^{-6}\,\mathrm{nm}^{-1}$. Therefore, it needs about 500 μm (i.e. $\sim 10^3$ periods) such that $|g_{\mathrm{Qu}}| \gtrsim 1$ *without external laser illumination*. This required interaction length has been successfully demonstrated recently [S31]. Note that in Ref. [S31], despite the coupling strength with the laser beam being around $g \sim 250$, the coupling strength with quantum vacuum $g_{\mathrm{Qu}} = g/\sqrt{N}$ (where N is the average photon number in the optical mode with which the electron interacts) was still low at $g_{\mathrm{Qu}} \approx 0.003$. Similar distinction between g and g_{Qu} also appears in the quantum description of accelerators, e.g. see Ref. [S32]. The interaction strength can be further increased if the electron-structure separation can be made narrower, such as few tens of nanometers as considered in Ref. [S33].

Taken together, this calculation finds the interaction strength of an electron with the electromagnetic vacuum and enables us to quantify the back influence of the electromagnetic mode on the electron. $|g_{\mathrm{Qu}}| \sim 1$ means that the probability of spontaneous emission and of re-absorption are equal even for a single electron. The flatband scheme can potentially enable the nonperturbative strong-coupling regime $|g_{\mathrm{Qu}}| \gtrsim 1$ even using passive cavities under amenable experimental conditions. The addition of external laser pumping will boost ever higher coupling strength. This strong effect is made possible thanks to the flatband behavior.

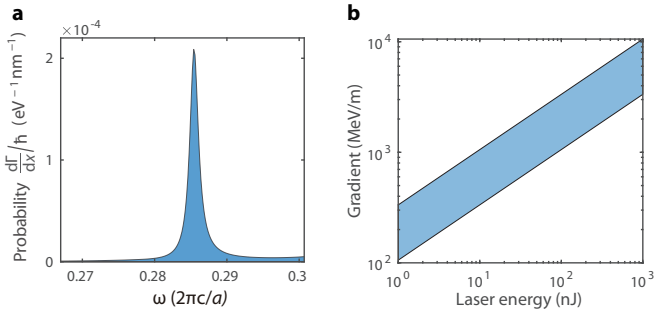

Figure S15. **Strong interaction enabled by the flatband scheme.** Emission probability (**a**) and Acceleration gradient (**b**) from the flatband resonances of the photonic crystal slab (see Fig. 2) for an electron-structure separation of 100 nm. In b, shading takes account of coupling efficiency range 0.01 – 0.1 and the propagation distance is taken as 10 μm, a typical value for on-chip dielectric laser accelerators [S34].

We can convert the g_{Qu} metric into acceleration gradient G (in unit of $\mathrm{eV\,m}^{-1}$) that is more commonly used in the accelerator community:

$$G = g_{\mathrm{Qu}} \hbar \omega_0 \sqrt{N\kappa}/L, \tag{S19}$$

where ω_0 is the center frequency of the pumping laser, N is the photon number from the laser beam, κ is the coupling efficiency, and L is the coupling length. Assuming a moderate pumping energy ~ 100 nJ, our structure has the potential to achieve a strong gradient of $G \sim 2\,\mathrm{GeV\,m}^{-1}$. This acceleration gradient suggests intriguing prospects for flatband-based dielectric laser accelerators. Such an accelerator design may benefit from having a wide transverse area that can accommodate higher electron fluxes, relative to the narrow channels of current dielectric laser accelerator designs.

We note that the estimate above uses our specific experimental design (tailored for enhanced radiation under our measurement conditions, but not for acceleration) that could be sub-optimal (e.g. shallow etched structure for coupling with ≤ 40 keV electrons) . Future detailed studies and optimizations are needed to unleash the full potential of the flatband scheme for acceleration purposes.

In our SEM-based measurements, the quality of the electron beam (see Sec. S3) and its oblique incident angle precluded us from achieving the required small interaction separation and the long interaction distance to enter the strong-coupling regime. It will be enticing to pursue this direction with ultrafast electron microscopes where higher-quality electron beams are available.

References

* yiyg@hku.hk; chrc@mit.edu; Y. Y. and C. R.-C. contributed equally to this work.

[S1] Y. Yang, A. Massuda, C. Roques-Carmes, S. E. Kooi, T. Christensen, S. G. Johnson, J. D. Joannopoulos, O. D. Miller, I. Kaminer, and M. Soljačić, Nature Physics **14**, 894 (2018).

[S2] C. Roques-Carmes, S. E. Kooi, Y. Yang, A. Massuda, P. D. Keathley, A. Zaidi, Y. Yang, J. D. Joannopoulos, K. K. Berggren, I. Kaminer, *et al.*, Nature communications **10**, 1 (2019).

[S3] A. Massuda, C. Roques-Carmes, Y. Yang, S. E. Kooi, Y. Yang, C. Murdia, K. K. Berggren, I. Kaminer, and M. Soljačić, ACS Photonics **5**, 3513 (2018).

[S4] I. Kaminer, S. Kooi, R. Shiloh, B. Zhen, Y. Shen, J. López, R. Remez, S. Skirlo, Y. Yang, J. Joannopoulos, and M. Soljačić, Phys. Rev. X **7**, 011003 (2017).

[S5] L. Reimer, *Scanning electron microscopy: physics of image formation and microanalysis*, Vol. 45 (Springer-Verlag, 1998).

[S6] J. Goldstein, D. E. Newbury, D. C. Joy, C. E. Lyman, P. Echlin, E. Lifshin, L. Sawyer, and J. Michael, *Scanning Electron Microscopy and X-ray Microanalysis* (Springer Science & Business Media, 2012).

[S7] A. Khursheed, *Scanning electron microscope optics and spectrometers* (World scientific, 2011).

[S8] G. H. Jansen, Nuclear Instruments and Methods in Physics Research Section A: Accelerators, Spectrometers, Detectors and Associated Equipment **298**, 496 (1990).

[S9] M. Morita, T. Ohmi, E. Hasegawa, M. Kawakami, and M. Ohwada, Journal of Applied Physics **68**, 1272 (1990).

[S10] H. Cui, C. Wang, and G. Yang, Nano letters **8**, 2731 (2008).

[S11] S. Basu, B. J. Lee, and Z. M. Zhang, Journal of Heat Transfer **132**, 023301 (2010).

[S12] X. Zhang and D. Zhang, in *IOP Conference Series: Materials Science and Engineering*, Vol. 108 (IOP Publishing, 2016) p. 012020.

[S13] B. Brenny, T. Coenen, and A. Polman, Journal of Applied Physics **115**, 244307 (2014).

[S14] C. Kremers, D. N. Chigrin, and J. Kroha, Physical Review A **79**, 013829 (2009).

[S15] T. J. Seok, A. Jamshidi, M. Kim, S. Dhuey, A. Lakhani, H. Choo, P. J. Schuck, S. Cabrini, A. M. Schwartzberg, J. Bokor, *et al.*, Nano letters **11**, 2606 (2011).

[S16] C. Kittel, P. McEuen, and P. McEuen, *Introduction to solid state physics*, Vol. 8 (Wiley New York, 1996).

[S17] A. F. Oskooi, D. Roundy, M. Ibanescu, P. Bermel, J. D. Joannopoulos, and S. G. Johnson, Computer Physics Communications **181**, 687 (2010).

[S18] L. Schächter and A. Ron, Phys. Rev. A **40**, 876 (1989).

[S19] C. Luo, M. Ibanescu, S. G. Johnson, and J. Joannopoulos, Science **299**, 368 (2003).

[S20] H. Andrews and C. Brau, Phys. Rev. ST Accel. Beams **7**, 070701 (2004).

[S21] V. Kumar and K.-J. Kim, Phys. Rev. E **73**, 026501 (2006).

[S22] H. Freund and T. Abu-Elfadl, IEEE Transactions on Plasma Science **32**, 1015 (2004).

[S23] C. W. Hsu, B. Zhen, A. D. Stone, J. D. Joannopoulos, and M. Soljačić, Nat. Rev. Mater. **1**, 16048 (2016).

[S24] A. Cerjan, C. Jörg, S. Vaidya, S. Augustine, W. A. Benalcazar, C. W. Hsu, G. Von Freymann, and M. C. Rechtsman, Science advances **7**, eabk1117 (2021).

[S25] K. M. McPeak, S. V. Jayanti, S. J. Kress, S. Meyer, S. Iotti, A. Rossinelli, and D. J. Norris, ACS Photon. **2**, 326 (2015).

[S26] C. M. Sears, E. Colby, R. Ischebeck, C. McGuinness, J. Nelson, R. Noble, R. H. Siemann, J. Spencer, D. Walz, T. Plettner, *et al.*, Physical Review Special Topics-Accelerators and Beams **11**, 061301 (2008).

[S27] N. Rivera and I. Kaminer, Nature Reviews Physics **2**, 538 (2020).

[S28] A. Cerjan, C. W. Hsu, and M. C. Rechtsman, Physical review letters **123**, 023902 (2019).

[S29] O. Kfir, V. Di Giulio, F. J. G. de Abajo, and C. Ropers, Science Advances **7**, eabf6380 (2021).

[S30] A. B. Hayun, O. Reinhardt, J. Nemirovsky, A. Karnieli, N. Rivera, and I. Kaminer, Science Advances **7**, eabe4270 (2021).

[S31] R. Dahan, S. Nehemia, M. Shentcis, O. Reinhardt, Y. Adiv, X. Shi, O. Be'er, M. H. Lynch, Y. Kurman, K. Wang, *et al.*, Nature Physics **16**, 1123 (2020).

[S32] Y. Adiv, K. Wang, R. Dahan, P. Broaddus, Y. Miao, D. Black, K. Leedle, R. L. Byer, O. Solgaard, R. J. England, *et al.*, Physical Review X **11**, 041042 (2021).

[S33] X. Bendana, A. Polman, and F. J. G. de Abajo, Nano letters **11**, 5099 (2011).

[S34] N. V. Sapra, K. Y. Yang, D. Vercruysse, K. J. Leedle, D. S. Black, R. J. England, L. Su, R. Trivedi, Y. Miao, O. Solgaard, R. L. Byer, and J. Vučković, Science **367**, 79 (2020).